

# Molecular dynamics simulation of single asperity contact

Pil-Ryung Cha<sup>a,\*</sup>, David J. Srolovitz<sup>a</sup>, T. Kyle Vanderlick<sup>b</sup>

<sup>a</sup> Department of Mechanical and Aerospace Engineering, Princeton Institute for the Science and Technology of Materials, Princeton University, Princeton, NJ 08544, USA

<sup>b</sup> Department of Chemical Engineering, Princeton Institute for the Science and Technology of Materials, Princeton University, Princeton, NJ 08544, USA

Received 2 February 2004; received in revised form 7 May 2004; accepted 8 May 2004  
Available online 17 June 2004

## Abstract

We present a series of molecular dynamics simulations of single asperity contact and deformation that occurs as two rough surfaces are brought together, loaded and then separated. We monitor the force between the two surfaces, the total potential energy, the  $Q_6$  order parameter, the effective minimum contact radius and the conductance (using the modified Sharvin equation). The deformation is observed using the local bond order parameter. During loading, the force–displacement relation exhibits a sawtooth form, associated with repetitive generation and motion of partial dislocations and the concomitant creation and annihilation of stacking fault pyramids. Unloading is characterized by an extended elastic deformation regime followed by plastic deformation of a type that is distinct from that in loading. The qualitative features of the force, contact area and conductance versus displacement plots are in excellent qualitative agreement with experimental observations. The simulations and experiments both show that Johnson–Kendall–Roberts theory should not be applied to describe asperity loading, but is applicable to the case of unloading, where the deformation is nearly elastic.

© 2004 Acta Materialia Inc. Published by Elsevier Ltd. All rights reserved.

*Keywords:* Contact mechanics; Asperity contact; Plastic deformation; Molecular dynamics; Lattice-defects

## 1. Introduction

Many state-of-art microelectronic, photonic and MEMS devices are based upon or created using small-scale contacts. These include, for example, high frequency, microscale electromechanical switches [1] and nanopatterning of organic optoelectronic materials by contact adhesion, cold welding, and lift-off [2]. The initial stages of contact occur between asperities of micro- and/or nano-scope dimensions. As a consequence, understanding the processes that occur at the atomic level when two rough surfaces are brought into contact is fundamentally important for a wide range of problems including adhesion, contact formation, contact resis-

tance, materials hardness, friction, wear, and fracture. The centrality of single asperities in the fundamental micromechanical response of contact between two rough surfaces has long been recognized. Unfortunately, contact behavior in the presence of adhesion and mechanical load remains poorly understood, despite the long-standing research interest in this problem.

The micromechanical response and electronic transport properties of single asperity contacts have received significant experimental attention. A wide range of experiments has shown that the conductance of small contacts changes abruptly as a function of contact size. The contact size effect has been studied through the generation of wires via the extension of materials contacts using tip-based methods [3–7], a break-junction technique (BJ) [8], and by the strain-induced necking of wires in contact [9,10]. In STM experiments, the tip is brought into contact with the sample and the conductance is measured as the tip is retracted. In the BJ technique, a metallic wire mounted on a substrate is

\* Corresponding author. Present address: School of Advanced Materials Engineering, Kookmin University, 861-1, Chongnung-dong, Songbuk-gu, Seoul 136-702, Republic of Korea. Tel.: +82-291-046-56; fax: +82-288-852-84.

E-mail address: [cprdream@kookmin.ac.kr](mailto:cprdream@kookmin.ac.kr) (P.-R. Cha).

stretched to breaking as the substrate is bent. As the substrate is repeatedly loaded and unloaded, contact is broken and re-established, albeit in a highly irreversible manner. Similar jumps in conductance have been observed in the final stages of separation of macroscopic metal bodies [9,10]. More recently, the conductance and force have been measured simultaneously using a STM supplemented by a force sensor [4–6]. These experiments demonstrated a clear correlation between jumps in the force and jumps in the conductance. This suggests that the widely observed jumps in conductance are related to highly localized deformation events.

Molecular dynamics (MD) simulations have been performed to look at these electronic and mechanical responses. The first set of simulations focused on the mechanical deformation and conductance of nanowires as they are stretched to breaking. The conductance was measured based upon tight-binding [11,12], a free-electron [7,12], or modified Sharvin [10,13] models. Jumps in conductance were found to be associated with atomic rearrangements where sudden structural and cross-sectional area changes occur, in agreement with recent combined force and conductance measurements [4,5]. The second type of simulation focused primarily on the mechanical response of an initially flat substrate during indentation with a hard, nanoscale indenter [14–18]. The force–displacement curves showed relatively abrupt force drops associated with the generation of dislocations [16,18]. Landman et al. [10] combined nano-indentation studies with the calculation of conductance. They found that the conductance jumps were correlated with structural transformations involving elastic deformation and yielding.

Although interesting, none of these studies address the deformation and conductance changes that occur when two arbitrary surfaces are brought into contact and then separated. As discussed above, the early stages of such contacts and the final stages of separations are controlled by well-separated asperities. Unlike indentation using hard indenters, in which the deformation occurs largely in the substrate, this type of deformation occurs largely within the asperities. In asperity deformation, dislocation can escape through the sides of the asperities and the remaining deformation will be focused toward the center of the asperity (rather than expanding outward as in the case of nano-indentation). Many of the earlier MD studies were performed under conditions where the contact size is very small. In such cases, the deformation was described as local atomic rearrangements, but the type of rearrangements that occurred could not be resolved. In the cases in which the contact size was in excess of 1 nm, clear evidence of dislocation motion was observed [10,13]. Therefore, the type of deformation (or at least the ability to resolve it) depends on asperity size. Recent experiments have used conductance measurements to estimate typical single as-

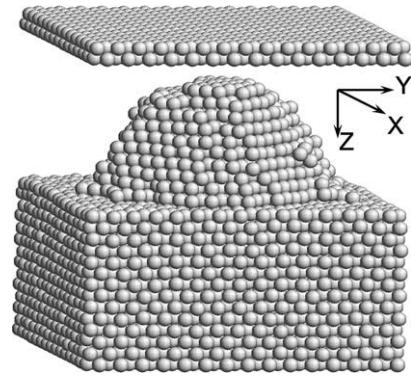


Fig. 1. The annealed asperity – rigid plate geometry.

perity contact radii and found them to be in the 1–8 nm range [5]. Few contact simulations have been performed on this scale and, of these, relatively little information was extracted on the nature of dislocation dynamics.

In the present work, we report the results of molecular dynamics simulations of single asperity contact during loading and unloading at room temperature. We focus on the mechanisms by which contact deformation occurs and the relationship between contact conductance (and contact area) and the deformation. The present simulations account for adhesion, elastic deformation, dislocation generation and migration, the formation of other types of defects and morphology evolution. In order to study the elastic and plastic deformation of the asperities on a rough surface, we set-up a model system, as shown in Fig. 1. For simplicity, we consider a single deformable asperity on a deformable substrate that interacts with a flat, rigid plate. We calculate the conductance of the contact during loading and unloading through the modified Sharvin model [12]. To our knowledge, this study represents the first dynamic, atomistic simulation of the elastic and plastic deformation behavior of a single asperity and the corresponding evolution of the contact area and contact conductance. The present simulation results reproduce a large body of existing nano-contact experimental results, including the stepwise variation of contact area and conductance with displacement and the hysteresis in the contact radius and contact resistance versus force curves.

## 2. Simulation methods

We use the MD technique to simulate the motion of atoms by numerically integrating Newton's equations of motion using the velocity-Verlet algorithm [19]. The inter-atomic interactions are described using the embedded-atom-method (EAM) [20,21] potential for Au developed by Cai and Ye [22]. The molecular dynamics simulations were performed constant number of atoms

( $N$ ), pressure ( $P$ ), and temperature ( $T$ ) – i.e., in the NPT ensemble.

The MD simulation cell is composed of two parts: a rigid plate and a flat deformable substrate containing 14 face centered cubic (002) planes of dynamic atoms upon which an asperity sits. Periodic boundary conditions are employed in the [100] and [010] directions and the simulation cell edge length in these is  $\sim 6.1$  nm. In order to obtain a realistic asperity configuration, we initially construct a cubic  $4\text{ nm} \times 4\text{ nm} \times 4\text{ nm}$  asperity on the surface containing 1280 atoms followed by two thermal annealing cycles. In the first cycle, we raise the temperature from 0 to 700 K in 10 ps, anneal at 700 K for 1 ns and cool to 0 K in 10 ps. Next, we raise the temperature from 0 to 300 K in 10 ps and anneal the sample for 5 ns (all of the simulations described below are performed at 300 K). The atomic configuration of the system following this thermal treatment is shown in Fig. 1. This is the state of the asperity at the beginning of the contact simulations described below. The total number of atoms in the system is 8480 and the average radius of the asperity is approximately 3 nm.

In the contact simulations, the plate is displaced in the [001] direction, towards the asperity and substrate. The atoms in the plate are fixed, except for the rigid translation of the plate. The initial separation between the plate and the top of the asperity is approximately 0.8 nm. During the contact simulations, we decrease or increase the separation between the substrate and rigid plate by  $0.005\text{ \AA}$  every 0.5 ps (i.e., 100 MD steps) such that the rate of loading and unloading is 1 m/s. Since this is a displacement controlled contact experiment using a perfectly rigid testing machine, the overall displacement is prescribed and the  $Z$ -component of the force on the plate is calculated during the simulation. The evolution of the defect structure is monitored using a local atomic structure analysis and the electrical conductance is calculated from the asperity-plate contact size throughout the simulation.

### 2.1. Local atomic structure analysis

During the loading and unloading cycles imposed by the displacement of the rigid plate, the asperity and substrate deform – generating a variety of point and line defects. Since we will describe the deformation behavior in terms of the generation and movement of these defects, proper identification of the defects is important. The nature of the defects can be determined through the local arrangement of atoms. For example, a stacking fault generated by the slip of a partial dislocation along a  $\{111\}$  plane can be recognized as a pair of hexagonal close packed (HCP) atomic layers within the face centered cubic (FCC) matrix. A dislocation can be recognized as a pattern of atoms containing less than 12 nearest neighbors.

During the MD simulations, we obtain the positions and momenta of all the atoms in the system at each time step, and therefore all possible descriptions of the evolution of the atomic structure are, in-principle, available. In this work, we use the bond-order parameter method to identify the local structure around each atom as well as the global structure of the system [23]. The local structure around atom  $i$  is determined by the second-order invariant local order parameter [23]

$$q_l(i) = \left[ \frac{4\pi}{2l+1} \sum_{m=-l}^l |q_{lm}(i)|^2 \right]^{1/2}, \quad (1)$$

where  $q_{lm}(i) = [\sum_{j=1}^{N_{\text{nb}}(i)} Y_{lm}(\vec{r}_{ij})] / N_{\text{nb}}(i)$ , where  $Y_{lm}$  are spherical harmonics,  $\vec{r}_{ij}$  is the unit vector connecting atom  $i$  with its neighboring atoms  $j$  that are within a given radius  $r_{\text{cut}} = 0.35$  nm (i.e., between first and second neighbors in the zero-pressure FCC lattice) from  $i$ , and  $N_{\text{nb}}(i)$  is the number of neighbors within  $r_{\text{cut}}$  of atom  $i$ . The first non-zero value of  $q_l(i)$  occurs at  $l = 4$  for atoms with cubic local symmetry. The values of  $q_4(i)$ ,  $q_6(i)$ , and  $q_8(i)$  are listed in Table 1 for different local environments: FCC, HCP, BCC, icosahedral, and decahedral. Based upon the values of these parameters, we can distinguish between the perfect crystal, stacking faults, dislocations, interstitials, and vacancies.

### 2.2. Contact radius and conductance

Based on the atomic configurations generated by the MD simulations, we determine the effective minimum asperity radius during loading and unloading. To calculate the effective minimum contact radius, we identify the (001) atomic plane in the asperity with the smallest cross-section area by projecting the atomic coordinates onto the  $X$ - $Y$ -plane, and calculate the effective minimum contact radius  $a_{\text{min}}$  using the expression (designed to yield the correct radius for a circular geometry) [24]

$$\frac{a_{\text{min}}^2}{2} = \frac{\sum_i [(x_i - x_c)^2 + (y_i - y_c)^2]}{N}. \quad (2)$$

Here, the sum is over all the atoms in the (001) atomic plane with the smallest cross-sectional area,  $N$  is the number of these atoms,  $x_c$  and  $y_c$  are the  $X$  and  $Y$  coordinates of the center of mass of this group of atoms.

The conductance of a macroscopic contact is proportional to the contact radius and inversely

Table 1  
Values of  $q_4(i)$ ,  $q_6(i)$ , and  $q_8(i)$  for different local configurations

Structure	Neighbor	$q_4(i)$	$q_6(i)$	$q_8(i)$
FCC	12	0.191	0.575	0.404
HCP	12	0.097	0.485	0.317
Decahedral	12	0.053	0.430	0.139
Icosahedral	12	0	0.663	0
BCC	14	0.036	0.511	0.429

proportional to the resistivity of the material [25]. However, if the dimensions of the contact are smaller than the mean free path of the electrons (of the order of 40 nm in Au at room temperature and much larger at lower temperatures) the conductance is proportional to the contact area, as described by Sharvin [25]. Using the corrected Sharvin equation [12,26], the conductance  $G_S$  of a contact of small radius  $a$  is given by

$$G_S = \frac{2e^2}{h} \left( \frac{A\pi}{\lambda_F^2} - \frac{P}{2\lambda_F} \right), \quad (3)$$

where  $e$  is the electron charge,  $h$  is Planck's constant,  $\lambda_F$  is the Fermi wavelength (for Au,  $\lambda_F = 5.19$  Å),  $A$  is the contact area and  $P$  is the perimeter of the contact. Although Eq. (3) provides a reasonably accurate estimate of the contact conductance, it is difficult to apply since the contact is never perfectly circular in the MD simulations (the perimeter and contact area are not easily identified). To work around this difficulty, we can recast Eq. (3) in terms of the minimum effective contact radius (obtained from Eq. (2)) using the calibrated form of the contact conductance proposed in [12]. The calibrated contact conductance is

$$G_S = \frac{2e^2}{h} \frac{(k_F a_{\min})^2}{5.8}, \quad (4)$$

where  $k_F$  is the Fermi wave vector and  $a_{\min}$  is the effective minimal contact radius corresponding to that of Eq. (2). Eq. (4) was obtained [12] through fitting tight-binding and exact free electron calculation data on the conductance of an atomic-scale metallic contact. The calibrated contact conductance was shown to be insensitive to the shape of the contact cross-section [12].

### 3. Contact and loading

The rigid plate, initially 0.8 nm above the top of the asperity, is slowly advanced toward the substrate at a fixed rate during loading. Fig. 2 shows the normal force on the rigid plate, the averaged total potential energy per atom, the average or global order parameter  $Q_6 = \frac{1}{N} \sum_{i=1}^N q_6(i)$ , the effective minimum contact radius  $a_{\min}$ , and the calibrated contact conductance  $G_S$  versus displacement. The zero of displacement corresponds to the initial separation between the rigid plate and the asperity. The sign of the force is negative when the rigid plate is attracted toward the substrate.

The force varies in a non-monotonic fashion with the displacement, exhibiting several force drops, which corresponds to some type of mechanical instability (see below). The initial force drop (labeled S) corresponds to the asperity jumping into contact with the rigid plate. The magnitude of the force drops alternate between small and large: small drops (B–C, F–G, J–K in

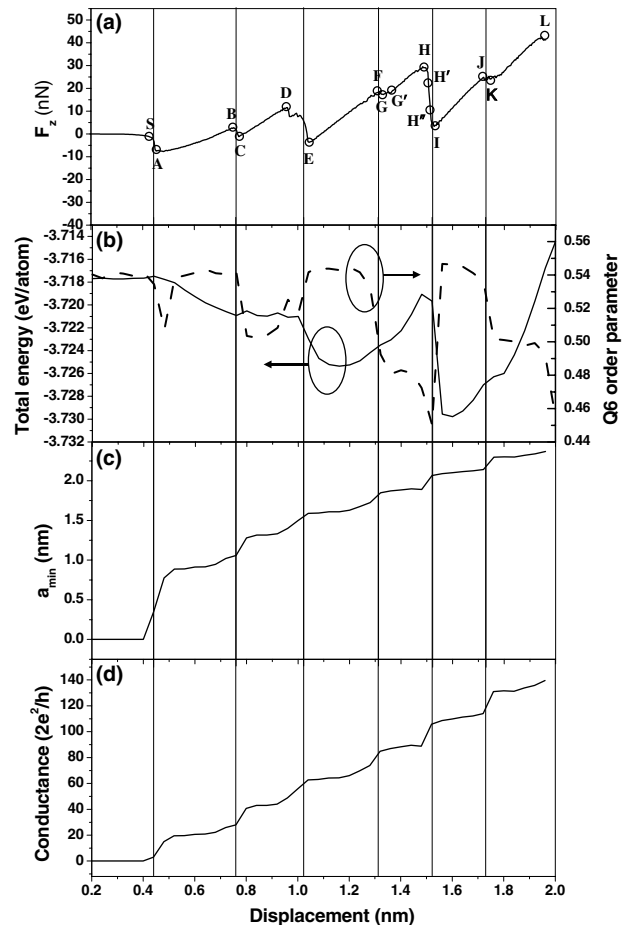


Fig. 2. The (a) calculated force,  $F_z$ , (b) total potential energy (solid line) and  $Q_6$  order parameter (dashed line), (c) effective minimum contact radius,  $a_{\min}$ , and (d) conductance,  $G_S$ , as a function of the displacement (measured from the initial separation between the substrate surface and the rigid plate) during loading. The letters label displacements discussed in the text and the vertical lines are at the approximate locations of force drops and are guides for the eye. Each value of  $F_z$  is an average over 4 ps, corresponding to a displacement of 0.04 Å, whereas the data for  $Q_6$ ,  $a_{\min}$  and  $G_S$  was calculated from a single atomic configuration each 0.4 Å.

Fig. 2(a) correspond to the nucleation of partial dislocations on four  $\{111\}$  different slip planes and the large drops (D–E, H–I) to the annihilation of the partial dislocations and stacking faults formed during the preceding small force drops. This will be discussed in more detail below. It is also possible to detect structural changes during deformation using the  $Q_6$  order parameter (Fig. 2(b)).  $Q_6$  order parameter drops abruptly at the displacement where the small force drops are observed (Fig. 2(a)). This can be traced to the generation of stacking faults (layers of HCP) generated by the motion of the first set of partial dislocations. These drops are followed by rapid increases at the same displacements where the large force drops were observed in Fig. 2(a). These are associated with the annihilation of the stacking faults, which restores the material to its

stacking fault-free state and the original value of  $Q_6$ . It is worth noting that total potential energy of the system increases slightly at those displacements corresponding to the small force drops, but remarkably shows a strong decrease at the displacements corresponding to large force drops. This means that the stacking faults structure generated at the small force drops raise the total potential energy of the solid. However, the thermodynamic driving force for structural change is the total energy plus the work done by the loading. This indeed must decrease when the first set of partial dislocations forms and propagate. If the applied load is removed, however, these partial dislocations will run out of the asperity. On the other hand, the large total potential energy drops occurs at the displacements where large force drops are observed, suggesting that the annihilation of the partial dislocations and stacking faults is an irreversible process. Finally, we note that both the small and large force drops correlate with the disappearance of a single (002) plane from the asperity.

Figs. 2(c) and (d) show that both the contact radius and conductance increase with increasing displacement in a stepwise manner. The constancy of the contact radius and conductance between force drops suggest that these stages of the deformation are predominantly elastic and the abrupt changes observed at force drops correspond to plastic deformation that changes the asperity radius. This is consistent with earlier experiments [4–10] and MD simulations [10–13] that suggested that the observed abrupt changes in contact conductance are the result of some type of mechanical instability.

At large separation,  $F_z \sim 0$  because the atomic interactions are short-ranged. As the separation between plate and asperity decreases, the two surfaces begin to weakly attract one another (from a displacement from  $\sim 0.3$  to  $\sim 0.4$  nm in Fig. 2(a)). When the displacement is increased only slightly more (beyond  $\sim 0.4$  nm), the force becomes strongly negative. This corresponds to the widely observed jump-to-contact instability. While jump-to-contact could occur purely elastically, observation of the surface of the asperity shows that some change in asperity shape occurs at this point [27]. These change are, however, limited to within a few Ås of the point of nearest asperity-rigid plate contact (this produces the drop in the  $Q_6$  order parameter at this displacement). The jump-to-contact produces a jump in the conductance from zero (neglecting tunneling) to 20 in units of  $2e^2/h$ , indicating that a connective neck between asperity and plate has been established. This conductance jump is very nearly equal to that observed in experiment (i.e., a jump of between 10 and 30 in the same units) [6].

We now address the issue of the microscopic origin of the small force drops observed in Fig. 2(a) (B–C, F–G, and J–K). Associated with the abrupt drop in the force (by less than 10 nN), there is a corresponding rapid drop

in the  $Q_6$  order parameter and a slight increase in the total energy at very nearly the same displacement (as described above). To illustrate the microscopic, structural origin of these rapid changes, we examine the atomic structure of the system (Fig. 3) at the displacements labeled F, G and G' in Fig. 2(a). The left and right columns of images in Fig. 3(a) show the atomic configurations of two slabs of atoms cut from the center of the model with  $[\bar{1}10]$  and  $[\bar{1}\bar{1}0]$  normals, respectively. Each slab nearly bisects the asperity and contains three adjacent  $\{110\}$  planes of atoms. Fig. 3(b) shows the atomic structure corresponding to the point G' in the  $[00\bar{1}]$  direction, where all atoms that exhibit a local FCC environment were removed from the image for the sake of clarity. The top row of images in Fig. 3(a), corresponding to the displacement F (see Fig. 2(a)), show that there are no dislocations in the system at this loading.

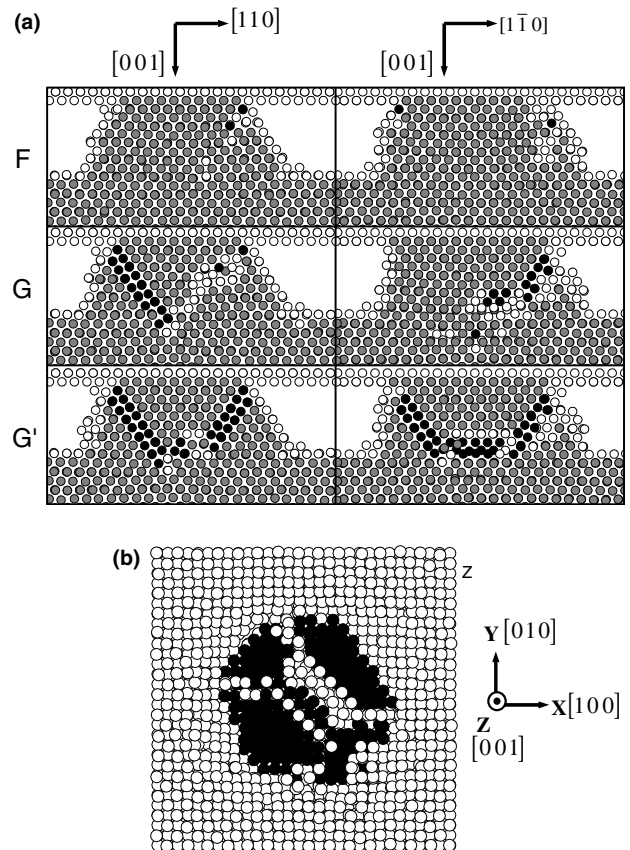


Fig. 3. (a) Atomic configurations of thin plates (three  $\{110\}$  atomic planes thick) cut from the simulation cell and through the center of the asperity. The images on the left and right correspond to  $[\bar{1}10]$  and  $[\bar{1}\bar{1}0]$  thin plate orientations, respectively. The labels F, G, and G' refer to Fig. 2(a). The atoms are colored according to their local structure as determined by the local bond order parameter: FCC order – gray, HCP order – black, and atoms with less than 12 nearest neighbors – white. (b) Atomic configuration seen from the  $[00\bar{1}]$  direction looking from the substrate toward the rigid plate, where all atoms with local FCC order were removed for clarity. This case corresponds to the displacement labeled G' in Fig. 2(a).

As the load is increased, partial dislocations nucleate on four different  $\{111\}$  planes (see the figures corresponding to G and G'). The Burgers vector of the dislocation on the  $(111)$  plane is  $a_0/6[\bar{1}\bar{1}2]$ ,  $a_0/6[\bar{1}\bar{1}2]$  on  $(\bar{1}\bar{1}1)$ ,  $a_0/6[112]$  on  $(\bar{1}11)$ , and  $a_0/6[112]$  on  $(1\bar{1}1)$ . Partial dislocations on crossing slip planes meet and generate stair-rod dislocations according to the reactions:

$$a_0/6[\bar{1}\bar{1}2] + a_0/6[\bar{1}\bar{1}2] \rightarrow a_0/3[\bar{1}02]$$

$$a_0/6[\bar{1}\bar{1}2] + a_0/6[1\bar{1}2] \rightarrow a_0/3[0\bar{1}2]$$

$$a_0/6[112] + a_0/6[\bar{1}\bar{1}2] \rightarrow a_0/3[012]$$

$$a_0/6[112] + a_0/6[1\bar{1}2] \rightarrow a_0/3[102]$$

The black atoms in Fig. 3(b) are at stacking faults. The stacking faults planes meet to create a pyramid-like shape (hereafter, referred to as a stacking fault pyramid (SFP)) that is delimited by lines of white atoms that correspond to stair-rod dislocations. These SFP remains stable as the load is increased. However, if the load is removed, the SFP disappears. The stair-rods formed by the reaction of the partial dislocations are unstable because their line tension is larger than the sum of those of the reacting two partial dislocations in the absence of an external stress. The stair-rods form as a result of the motion of the partials that are driven by the applied loading. This explains why the total potential energy of the system slightly increases during the formation of the SFP. This further explains why these structures have not been observed experimentally (removal of the load allows the stair-rod dislocations to retract). The SFP is a unique feature of the deformation of an asperity on  $\{001\}$  surfaces and is a result of the orientation of the available slip planes and the focusing of the deformation (i.e., convergence of the slip) within the asperity. Examination of Fig. 3(a) demonstrates that the formation of the SFP also correspond to the disappearance of a single  $(002)$  atomic plane (cf. the images corresponding to F and G' in Fig. 3(a)).

We now examine the mechanisms underlying the large force drops at D–E and H–I in Fig. 2(a), which occur following the small force drops (B–C and F–G). Normally, one would expect that further loading would generate more defects and more dislocations after the formation of SFP at the small force drops. To examine this issue, we plot the atomic configurations (see Fig. 4) corresponding to the displacements H, H', H'', and I (in Fig. 2(a)). The viewing angles for these figures are the same as for Fig. 3(a). The top row of images in Fig. 4 (displacement H) shows a single SFP akin to that seen in the third row of images in Fig. 3(a). Upon further loading, new partial dislocations are generated near the corners of the asperity/rigid plate contact (displacement H') which travel along the  $\{111\}$  stacking faults left

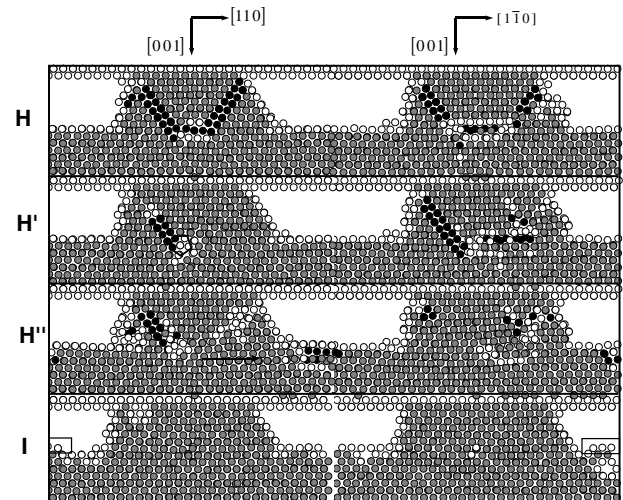


Fig. 4. Atomic configurations of thin plates (three  $\{110\}$  atomic planes thick) cut from the simulation cell and through the center of the asperity. The images on the left and right correspond to  $[\bar{1}10]$  and  $[\bar{1}\bar{1}0]$  thin plate orientations, respectively. The labels H, H', H'', and I refer to Fig. 2(a). The pentagon in the second row indicates the position of a full dislocation with Burgers vector  $[001]$ . The arrow represents the direction of motion of the  $[001]$  dislocation. The atomic layer marked with rectangular boxes in the lower figures shows the slip step produced during the annihilation of a stacking fault pyramid.

behind by the earlier set of partial dislocations. The new partials have Burgers vectors  $a_0/6[1\bar{2}1]$  on the  $(111)$  plane and with  $a_0/6[\bar{1}21]$  on the  $(\bar{1}\bar{1}1)$  plane at displacement H', as seen in the second row of images in Fig. 4. These two dislocations destroy the stacking faults left behind by the earlier partials (this process is not complete at displacement H'). The new partials and those generated earlier then react to produce perfect dislocations with Burgers vectors  $a_0/2[0\bar{1}1]$  and  $a_0/2[011]$ . These two dislocations then react to form a perfect dislocation with Burgers vector  $a_0[001]$  (see the fivefold symmetry structure in the second row in Fig. 4). At this time, the remaining two partial dislocations on the  $(\bar{1}11)$  and  $(1\bar{1}1)$  planes (seen in the right image in the second row of Fig. 4) glide to the surface and out of the solid (see the right image in the third row of Fig. 4 at displacement H''). Next, the  $a_0[001]$  dislocation glides along the  $(001)$  plane away from the region of high compression and dissociates into two sets of partials on two different slip planes, namely:  $a_0/6[\bar{1}\bar{2}1] + a_0/6[1\bar{1}2]$  on the  $(\bar{1}\bar{1}1)$  plane and  $a_0/6[121] + a_0/6[112]$  on the  $(1\bar{1}1)$  plane. This can be seen on the right-hand side (three planes below the substrate surface) of the left image in the third row (displacement H'') of Fig. 4. These partial dislocations then glide to the surface, effectively decreasing the height of the asperity by a single  $(002)$  plane of atoms (note the slip step in the box on the left-hand side of the left image in Fig. 4 at displacement I). When the  $a_0[001]$  dislocation glides to the right (left image at displacement H''), a new set of partial

dislocations form on the (111) plane near the corner of the asperity/rigid plate contact and a process akin to that described above occurs again.

Although the detailed dislocation mechanism involved in the large force drops are complex, a few salient features can be extracted: (1) partial dislocations form at the corner where the asperity and rigid plate meet, travel along and destroy the existing stacking fault and react with the partial formed earlier to create a perfect dislocation, (2) this dislocation undergoes several reactions, travels away from the asperity and then out the free surface, leaving a slip step and a dislocation free material, and (3) the generation and escape of the dislocations reduce the height of the asperity. The present results also show the detailed dislocation mechanism by which material from the asperity is transferred to nearby regions on the substrate surface. Similar observations have been made for nano-indentation [17].

#### 4. Unloading

Following loading to a displacement of 1.96 nm (displacement L in Fig. 2(a)), we begin reversing the displacement (i.e., retracting the rigid plate from the substrate/asperity). Fig. 5 shows the force, total potential energy, effective minimum contact radius and conductance versus the displacement for unloading. The atomic configuration corresponding to the displacement where the loading is reversed is shown in Fig. 6(a). At this displacement, a well-formed SFP extends into the substrate. In the early stages of unloading, the force and total potential energy decrease as the rigid plate is retracted. This is predominantly the elastic response to decreasing the load. Between displacements A and B in Fig. 5, the first force jump occurs. This corresponds to the annihilation of the SFP generated during loading. As described above, the SFP is stable only in the presence of the applied load. When that load is removed, the dislocation line tension leads to the dissociation of the stair rod dislocations and egress of the partial dislocations that constitute the edges of the SFP. As the rigid plate continues to be retracted, the sign of the force changes from compressive (positive) to tensile (negative). Further rigid plate retraction leads to another force jump between displacements C and E. As we will show below, this is associated with plastic deformation/dislocation slip albeit very different dislocation slip than occurred in loading. The maximum tensile force (corresponding to the pull-off force in a load-controlled experiment) appears to occur at displacement F in Fig. 5(a), however, if the data were not averaged, the true maximum tensile force would be observed at displacement C. With further retraction of the rigid plate, many new dislocations are generated and the defect density in the system continuously increases. The dis-

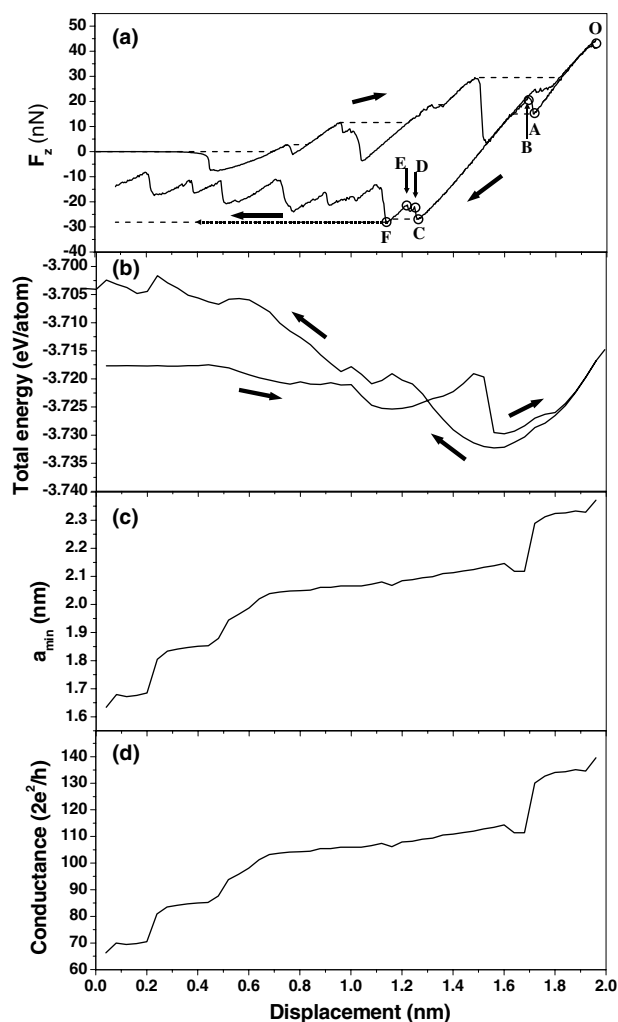


Fig. 5. The (a) calculated force,  $F_z$ , (b) total potential energy, (c) effective minimum contact radius,  $a_{\min}$ , and (d) conductance,  $G_s$ , as a function of the displacement (measured from the initial separation between the substrate surface and the rigid plate) during unloading and loading. The dashed curves in (a) indicate the force displacement relation corresponding to a force-controlled experiment, as discussed in the text.

placement at zero force corresponds to the minimum in the total potential energy of the system. The total potential energy is very nearly a quadratic function of the displacement near this point – further supporting the notion that between displacements B and C, the deformation is linear elastic (in fact it is elastic from O to C with the exception of the jump at A). The difference in the displacement between that of the initial jump-to-contact and that corresponding to the minimum in the total potential energy corresponds to the plastic displacement that occurred on loading (this includes the reversible dislocation motion that occurred at point A). Therefore, the plastic deformation that occurred on loading irreversibly decreased the height of the asperity by  $\sim 1.1$  nm or  $\sim 5$  (002) atomic planes (which is confirmed by comparing the atomic configurations of the

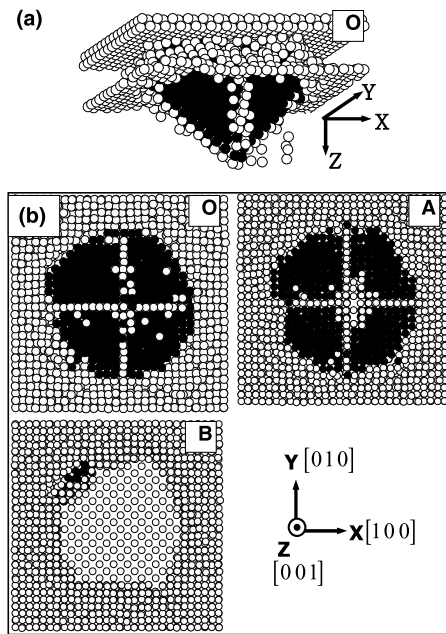


Fig. 6. (a) Atomic configuration at the displacement from which unloading is begun (displacement O in Fig. 5(a)). (b) Atomic configurations viewed from the [001] direction (looking from the substrate towards the rigid plate). The configurations correspond to the displacements labeled O, A, and B in Fig. 5(a). Atoms with local FCC order were removed for clarity, as per Fig. 3(b).

asperity prior to loading and at the minimum elastic energy on unloading).

As in loading, the effective minimum contact radius and conductance vary with displacement in a step-wise manner during unloading (see Fig. 5(c) and (d)). The first step seen upon unloading (displacement A in Fig. 5(a)) corresponds to the annihilation of the SFP that was formed during loading. Following this drop, further decrease in the displacement yields a slow, nearly linear decrease in the contact radius and conductance (displacements from 1.6 to 0.6 nm). The small, finite size of this slope is indicative of the elastic deformation of the asperity and the existence of a non-zero Poisson ratio. This small slope plateau spans several plastic events, implying those events do not modify the cross-section of the asperity. Indeed, in the long plateau observed in the contact radius and conductance versus displacement, the plastic deformation occurs in the substrate or near where the substrate meets the asperity (see Fig. 7), leaving the minimum cross-sectional area of the asperity nearly unaltered. However, further rigid plate retraction leads to plastic deformation that extends into the asperity, thereby decreasing the effective minimum contact radius and the conductance (e.g., note the three drops that occur between 0.6 and 0 nm).

We now examine the mechanism by which the SFP generated during loading is annihilated during unloading (between displacements A and B in Fig. 5(a)).

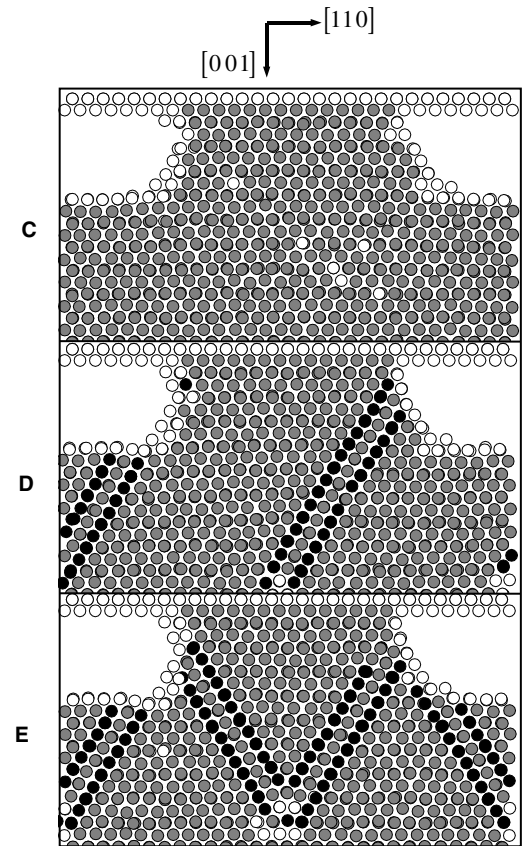


Fig. 7. Atomic configurations showing the generation of partial dislocations (the extrinsic stacking faults) during unloading. The configurations correspond to the displacements labeled C, D, and E in Fig. 5(a).

Fig. 6(b) shows the atomic configurations corresponding to displacements O, A, and B. These figures show that the partial dislocations that met at the apex of the pyramid move toward the free surface, thereby unzipping the stair-rod dislocations that form the edges of the SFP. In the image corresponding to B in Fig. 6(b), most of the partial dislocations have escaped out the surface and only a small segment remains near one edge of the asperity. The escape of these partial dislocations increases the height of the asperity by a single (002) atomic plane.

Following the long elastic retraction of the rigid plate from displacements B to C (Fig. 5(a)), another plastic deformation event occurs. This event is illustrated in Fig. 7, where we show the atomic configurations corresponding to displacements C, D, and E in Fig. 5(a). At displacement C, the asperity and substrate are dislocation-free. Further rigid plate retraction leads to the formation of a set of stacking faults that are very different from those formed during loading as seen in images (Fig. 7) corresponding to displacements D and E in Fig. 5(a). The stacking faults are composed of two HCP layers separated by an FCC layer. This is an extrinsic

stacking fault [28]. Slip first occurs on a (1 1 1) slip plane (image D in Fig. 7), followed by slip on the (1̄ 1 1) slip plane (image E in Fig. 7). Note, unlike in the loading case, all four (1 1 1) slip planes are never simultaneously active. The microscopic mechanism of extrinsic stacking fault formation is as follows. During the retraction of the rigid plate in the [0 0 1] direction, the maximum resolved shear stress (MRSS) on the (1 1 1) plane is in the [1 1 2̄] direction. Fig. 8(a) shows two adjacent (1 1 1) planes and the direction of the MRSS. During unloading, the lower layer would slip straight down relative to the upper layer in the geometry of this figure. If this happens, the dark atoms would lie directly beneath the white atoms, creating an extremely high energy stacking fault. This is shown in Fig. 8(b) using the traditional (1 1 1) plane stacking sequence notation for FCC metals. The formation of this stacking fault corresponds to the first column in Fig. 8(b) transforming to the second. Since the energy of this stacking fault is so high, it is unstable and decays to that shown in the third column in Fig. 8(b). The circle A and C layers in Fig. 8(b) have the classic alternating layer stacking of an HCP structure, while the intervening B layer retains the ABC stacking of an FCC structure. This is an extrinsic stacking fault. Note that during loading, the black atoms would slip up (rather than down) in Fig. 8(a). This would create the stable, low energy intrinsic stacking fault. This explains why intrinsic stacking faults are observed during loading and extrinsic stacking faults form during unloading. We can represent the formation of the extrinsic stacking fault that forms on unloading in terms of a partial dislocation reaction

$$a_0/6[1\ 1\ \bar{2}]^1 \rightarrow a_0/6[2\ \bar{1}\ \bar{1}]^1 + a_0/6[\bar{1}\ 2\ \bar{1}]^2 \quad (5)$$

where the superscripts 1 and 2 indicate that these dislocations are on adjacent, parallel (1 1 1) planes. These two partial dislocations move together.

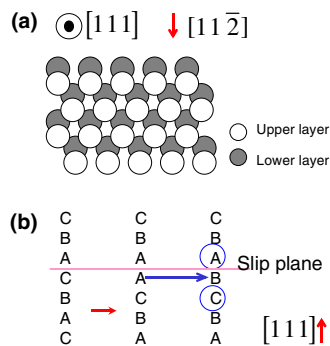


Fig. 8. Schematic illustration of the formation of an extrinsic stacking fault during unloading. (a) Schematic diagram of two atomic layers seen from [1 1 1] direction. [1 1 2̄] is the maximum resolved shear stress direction during unloading. (b) Changes in the atomic layer stacking sequence during the formation of an extrinsic stacking fault (see [28]). The circles indicate local HCP order.

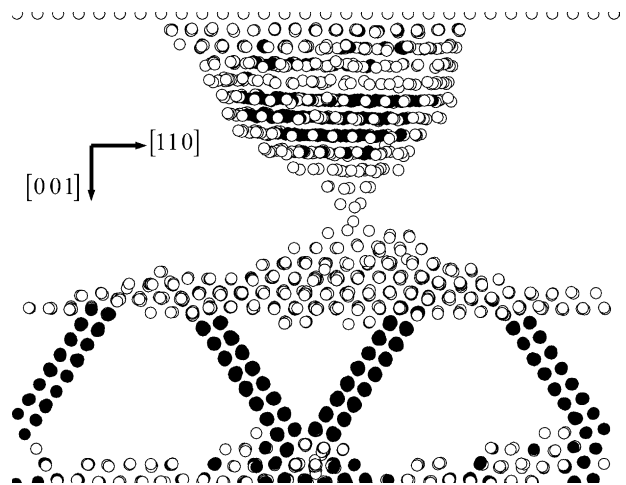


Fig. 9. Atomic configuration during unloading immediately prior to contact rupture.

Further unloading beyond displacement E in Fig. 5(a) generates increasing densities of dislocations both in the substrate and in the asperity, as shown in Fig. 9. This is quite different than observed during loading where further deformation repeatedly forms and annihilates dislocations such that the dislocation density oscillates.

Perhaps more interesting is that when the plate and substrate separate, a significant fraction of the atoms that were in the substrate have been transferred to the plate. This is further demonstration that asperity contact is an irreversible process. When the plate and substrate separate, a thin neck is formed between the transferred material and the substrate that eventually breaks. We note that when the rigid plate is retracted at a very high rate, this neck can be greatly extended, producing a wire of atomic radius between the plate and substrate. The formation of such wires was reported earlier in MD simulations of elongation of nanowire [13]. This suggests the degree to which wire formation occurs is very sensitive to the deformation rate.

### 5. Discussion

Agrait et al. [4,5] performed a series of experiments in which they brought a gold tip in contact with a nominally flat gold surface while simultaneously measuring the contact force and contact conductance. A representative set of experimental loading and unloading results at 300 K in ambient conditions is shown in Fig. 10 and the inset shows experimental set-up. These results show the presence of abrupt changes in both the contact force and contact conductance both on loading and unloading. In order to compare our simulation results with those obtained experimentally, we must account for the difference between the simulation and experimental

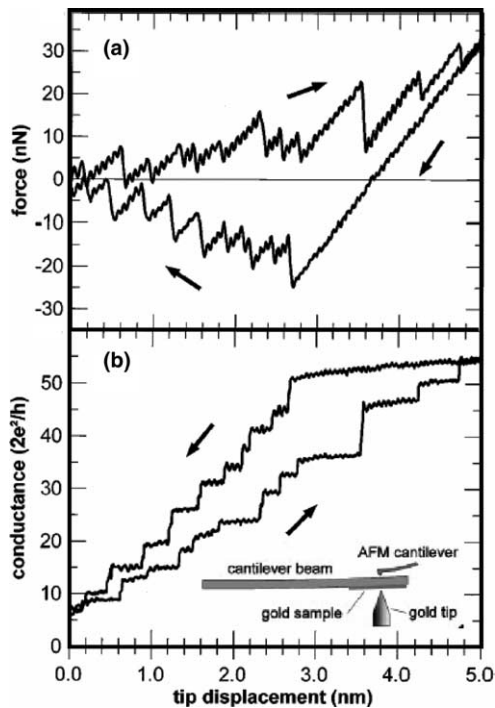


Fig. 10. Measured force and conductance versus displacement during a cycle of loading and unloading a Au contact at 300 K from [5]. The force is measured with a cantilever beam of effective spring constant of 35 N/m in the experimental geometry shown in the inset. This plot is reproduced from [5] with the permission of the authors.

geometry. More specifically, the experimental system used a very low stiffness test configuration, while the simulated contact study was performed using a very

high stiffness geometry. In particular, in the experiment [5], the force was applied through the deflection of cantilever beams with spring constants of 25 and 35 N/m. Such low spring constants were necessary in order to create measurable displacements for forces of order 1 nN. We can think of the experiment as pushing or pulling a spring attached to the rigid plate that is in contact with the tip (see the inset in Fig. 11(b)). The spring and the rigid plate correspond to the cantilever beam in the experiment. In order to transform the simulation results such that they are comparable with the experiment, we adopt the method proposed in [13]. The displacement of the upper end of the compliant spring and the displacement of the rigid plate are denoted  $Z_C$  and  $Z_R$ , respectively.  $Z_C$  is controlled in the experiment and  $F_z$  is measured as the force created by the spring. This force is  $F_z = k(Z_C - Z_R)$ , where  $k$  is the spring constant. In order to transform the simulation results to the experimental situation, we must relate  $F_z(Z_R)$  determined from the rigid test geometry simulations to  $F_z(Z_C)$ , corresponding to the compliant test geometry experiments. To obtain this mapping, we specify a value of  $Z_R$ , determine  $F_z(Z_R)$  from the simulation, and then calculate  $Z_C$  from the spring equation, i.e.,  $Z_C = Z_R + F_z(Z_R)/k$ .

The force and tip conductance simulation results are replotted in Fig. 11(b) following the transformation from  $Z_R$  to  $Z_C$  coordinates for the case of a spring constant of  $k = 35$  N/m. The new force–displacement plot can be characterized as a series of finite slope regions, separated by abrupt force drops (rises) in com-

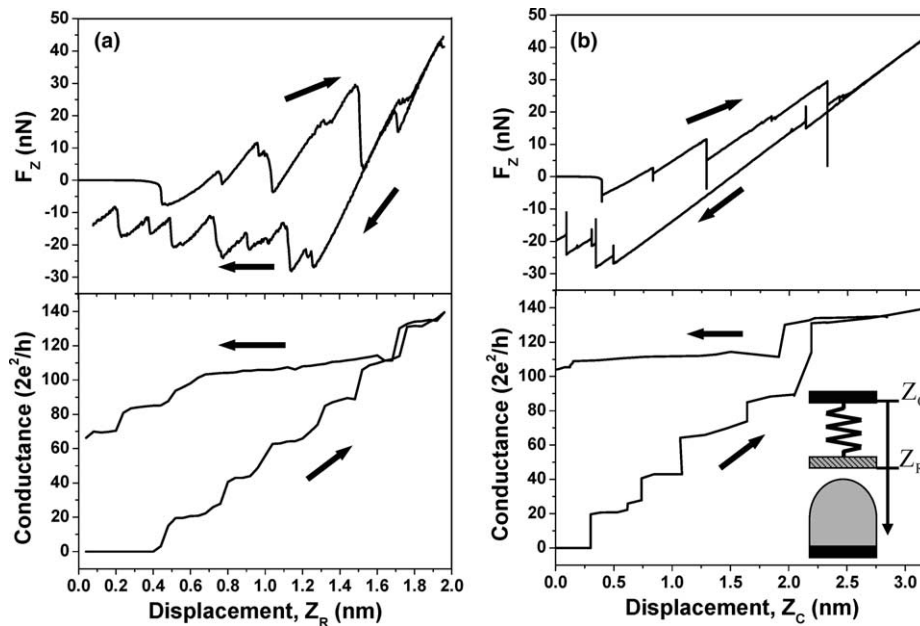


Fig. 11. The force versus displacement and conductance displacement curves obtained (a) from the simulation and (b) as modified to account for the small stiffness of the experimental cantilever geometry, as discussed in the text. The inset shows a schematic illustration of the approach used to convert between the effective displacements in the rigid ( $Z_R$ ) and compliant ( $Z_C$ ) test geometries.

pression (tension). The finite slope regions correspond to periods of elastic deformation. The abrupt force drops can be understood as follows: when the asperity undergoes plastic deformation such that its height decreases, the spring extends and hence the force drops. Since the plastic deformation is very fast relative to the rate at which the top of the spring is moved, the force drops in Fig. 11(b) appear as abrupt. More precisely, a vertical drop in  $F_Z(Z_C)$  (i.e., a mechanical instability) will occur when the slope of  $-F_Z(Z_R)$  is smaller than the spring constant,  $k$ .

We can now compare the simulation and experimental results on an equal basis. Like the experiment (Fig. 10(a)), the transformed simulated force–displacement curve (top image in Fig. 11(b)) shows finite slope regions separated by vertical force drops. In experiment and simulation, the unloading curves are characterized by an initially long elastic (constant slope) region, followed by a series of force jumps. The maximum tensile force in the simulation was approximately  $-30$  nN, while the experiment shows a maximum tensile force of approximately  $-25$  nN. While this excellent agreement is somewhat fortuitous, it is simply an indication that the local flow stress and contact area in the simulation and experiment are very similar. Both the experiments and simulation contact conductance plots show a combination of nearly vertical and horizontal segments. In both

cases, the drops in the conductance are well correlated with sharp drops/jumps in the force. The conductance is larger on unloading than during loading at the same displacement (simulation and experiment), indicative of the widening of the contact area during loading. The magnitude of the conductance is approximately two times larger in the simulation than in the experiment. This quantitative discrepancy may be the result of approximations inherent in the modified Sharvin equation or the existence of more scattering sites in the experiment than are accounted for in this equation. In fact, the simulation show that dislocations and stacking faults are generated in and around the asperity during both loading and unloading – a feature not accounted for in the analytical conductance equation.

The existence of hysteresis in contact radius versus force and contact resistance versus force (or corresponding applied voltage between the cantilever and the counter electrode in a MEMS switch) curves has been reported in experiments in which rough surfaces are pushed together and then pulled apart [29,30]. Fig. 12(a) shows the variation of the contact radius as a function of applied load in an experimental study of contact between a flat mica surface and a rough Au surface [29]. In this figure, the filled and open circles represent experimental data obtained upon loading and unloading, respectively, and the solid lines are theoretical curves

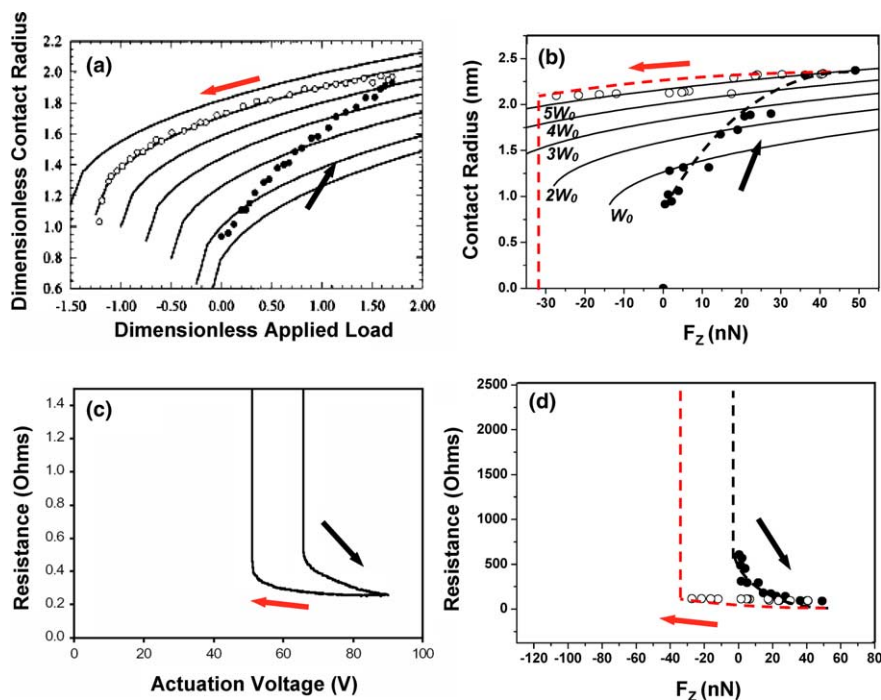


Fig. 12. (a) Measured dimensionless contact radius versus dimensionless applied load curve reproduced from [29], with permission. (b) The contact radius versus force curve from the simulations (in the force-controlled geometry, as discussed in the text). The dash lines guides for the eye. The solid lines in (a) and (b) represent the prediction of Johnson–Kendall–Roberts theory [31] with different values of the work of adhesion. (c) Measured contact resistance as a function of actuation voltage in a MEMS switch reproduced from [30], with permission. The actuation voltage is proportional to the force on the contact. (d) Simulated contact resistance versus force curve (force-controlled geometry). In all cases, the filled and open circles correspond to loading and unloading, respectively.

calculated using the classical theory of Johnson, Kendall and Roberts (i.e., JKR theory) [31] with different values for the ideal interfacial works of adhesion,  $W$ . JKR theory predicts that the contact radius  $a$  varies with asperity radius  $R$ , elastic constant  $K$ , and applied load  $P$  as [29,31]

$$a^3 = \frac{R}{K} \left[ P + 3\pi RW + \sqrt{6\pi RWP + (3\pi RW)^2} \right]. \quad (6)$$

Comparison of the experimental and theoretical results in loading demonstrates that JKR theory does not even provide a qualitative description of the compressive loading experimental data. On the other hand, the separation data closely matches the JKR prediction with a constant work of adhesion. Fig. 12(c) shows the contact resistance (inverse of the conductance) versus the applied actuation voltage curve [30] in a MEMS switch (a detailed description of the MEMS switch is in [32]), where the applied force is proportional to the actuation voltage. The resistance drops suddenly at a fixed actuation voltage (i.e., when the two surface are brought into contact) and then slowly decreases with further increase in the voltage. When the voltage decreases, the contact resistance increases very slowly before contact is lost at an actuation voltage lower than that required to bring the surfaces initially into contact. The decrease in contact resistance with applied voltage is attributable to increasing contact area as the compressive force is increased. The contact radius and resistance plots (Figs. 12(a) and (c)) are related through the modified Sharvin equation that suggests that the contact resistance is inversely proportional to the square of the contact radius.

Before comparing the contact radius and resistance versus applied load results from our MD simulations with the experimental results in Fig. 12(a) and (c), we must convert the results of our displacement controlled simulations to the force controlled case employed in the experiments [29,30]. This can be done simply. Since in the force-controlled case, the force can only increase and never decrease (during loading), we traverse the force–displacement curve obtained from the displacement controlled simulation (e.g., Fig. 2(a)) and anytime the force decreases, we simply allow the displacement to jump to the next point on the curve with the same value of the force. This ensures that the force–displacement curve in loading is monotonically increasing. The force controlled force–displacement curve is shown as the dashed lines in Fig. 5(a). The jump-to-contact and those corresponding to plastic deformation appear as jumps in displacement. The same procedure can be applied to the unloading case except that the jumps in displacement are in the opposite direction. This procedure leads to a much smoother force–displacement curve than that shown in the displacement-controlled case, albeit with jumps in displacement (Fig. 5(a)). On unloading, there will be a jump to infinite separation when the applied

tensile force exceeds the maximum tensile force in the displacement-controlled plot (point C or F in Fig. 5(a)). This jump to infinity occurs at the end of the reversible deformation region on unloading, as discussed above.

Figs. 12(b) and (d) show the contact radius versus force and contact resistance versus force curves corresponding to the force-controlled conditions, as described in the previous paragraph. There is clearly hysteresis on loading and unloading, indicative of non-elastic deformation. The solid lines in Fig. 12(b) are the predictions of the JKR theory with different values of the interfacial work of adhesion. On loading, the data cuts across the different JKR curves, while on unloading, the data is reasonably well described by the JKR theory with a constant interfacial work of adhesion. The reason JKR theory appears to work so well on unloading is that the deformation between points O and C is elastic, except for the single even between A and B in Fig. 5(a). Since plastic deformation occur in many steps in the loading curve between the initial jump-to-contact and point O, the assumption of elastic deformation inherent in the JKR theory is inappropriate and JKR theory is inapplicable. We have attempted to determine the interfacial work of adhesion from Eq. (6) and Fig. 12 using the appropriate value of the constants ( $R \approx 3$  nm and  $K = 63.76$  GPa) and obtained  $W \approx 6830$  mJ/m<sup>2</sup>. Ideally, the interfacial work of adhesion for this case should be twice the {001} surface energy or  $W_0 = 1366$  mJ/m<sup>2</sup> [22]. The interfacial work of adhesion obtained from fitting the simulations to the JKR theory is approximately five times larger than this. This discrepancy may be largely attributed to the fact that the asperity is not hemispherical (especially after the plastic deformation that occurs on loading). On the other hand, the initial point of contact lies much closer to the  $W = W_0$  curve (Fig. 12(b)). This is presumably because the initial asperity shape prior to loading is close to hemispherical. Since the contact conductance is a function of the contact radius (Eq. (4)), the dependence of the contact resistance on loading provides another measure of the evolution of contact size during loading and unloading. Using the force–displacement relation from Fig. 5(a) for the force-controlled case and the modified Sharvin equation (Eq. (4)), we can determine the contact resistance as a function of applied load for the same type of experiment as in Fig. 12(c). The results, plotted in Fig. 12(d), show excellent correspondence with the experimental measurements reproduced in Fig. 12(c).

Previous MD simulations of nano-indentation [16] have reported multiple force drops occurring during the indentation of a crystal using a hard indenter. These drops were associated with the nucleation and propagation of dislocations. These simulations showed that as the depth of the indentation increases, the dislocations/defect densities continuously increase and no recovery of the structure back to the dislocation-free state was ob-

served. The stacking faults generated on indentation are either parallel or splay outward from the indentation. These observations are in sharp contrast to the present simulations where the deformation is limited to the asperity and its substrate. In particular, during loading of the asperity, dislocations and stacking faults are repeatedly generated and annihilated and the stacking faults generated focus to produce the observed stacking fault pyramids. Each stacking fault annihilation event in the asperity loading simulations was associated with large force drops. This is quite distinct from the force drops seen in the nano-indentation simulations where they were only associated with dislocation nucleation. Hence, it is not appropriate to extrapolate from the nano-indentation case to understand asperity deformation in compression, despite the apparent similarities in geometry.

We performed a series of preliminary simulations of asperity contact for the case of (1 1 1) oriented asperities. This was designed to get an initial idea of how much asperity orientation affects the deformation behavior. For the asperity on the {001} surface, the force–displacement curve shows repetitive small and large force drops corresponding to the generation and annihilation of stacking fault pyramids (composed of intrinsic stacking faults on four {111} slip planes) during loading, the loss of one {002} atomic plane in each force drop cycle, and dislocations extending into the substrate. In a similar manner, the compressive deformation of an asperity on the {111} surface also produces periodic force drops that correspond to the disappearance of one {111} atomic plane in the asperity and deformation localized to the asperity region. However, because of the difference in the orientation of the slip planes in the two cases, the stacking fault pyramid observed in the {100} case does not appear in the {111} case. While the unloading of the {001} asperity generate extrinsic stacking faults, unloading the {111} asperity produced intrinsic stacking faults. The main conclusion from this comparison is that the general features of the observations made in the {001} case (the focus of this paper) are robust upon change of asperity orientation (however, the detailed deformation mechanism may be quite different).

Finally, we briefly consider the effects of asperity size and substrate thickness in our simulations. To this end, we performed a preliminary series of simulations in which we increased the substrate thickness by a factor of two at fixed asperity size. The results showed that the same type of deformation behavior occurred in both cases, albeit the deformation events occurred at slightly larger displacement in the thicker substrate case. This delay is associated with the decrease influence of the rigid layer at the bottom of the substrate as the substrate thickness is increased. This is not surprising since the rigid layer provides some constraint on the deformation

(even though the depths to which the dislocations penetrated into the substrate is similar for both substrate thicknesses). We also performed a preliminary simulation with both smaller ( $\sim 1.5$  nm) and larger ( $\sim 6$  nm) radius asperities (the simulations discussed above used  $\sim 3$  nm asperities). The  $\sim 6$  nm asperity exhibited the same deformation mechanisms as did the  $\sim 3$  nm asperity. However, the plastic deformation of the  $\sim 1.5$  nm asperity produced no stacking fault pyramid and was only localized to within the asperity at small displacements. At larger displacement, the deformation continuously increases the defect density in the substrate, with no recovery to the dislocation-free structure. Hence, while asperities of size greater than a few nm behave similarly, the deformation of very small asperities may be different. This may be associated with the fact that such asperities become comparable with dislocation core sizes and hence well-formed dislocations may not exist.

## 6. Conclusion

We presented the results of a molecular dynamics simulation of single asperity contact and deformation as two surfaces are brought together, loaded and then separated. We monitored the force between the two surfaces, the total potential energy, the  $Q_6$  order parameter, and the effective minimum contact radius. The latter was used, together with the modified Sharvin equation to estimate the conductance of the contact during asperity deformation. The local bond order parameter [23] was used to identify the formation and motion of defects (stacking faults, dislocations, and vacancies) during the loading and unloading cycle. During loading, the force–displacement relation exhibited sawtooth features, associated with repetitive generation and motion of partial dislocations and the concomitant creation and annihilation of stacking fault pyramids. The plastic deformation corresponding to each force drop induced a discrete change in the thickness of the asperity, its effective radius and the conductance of the contact. Upon unloading, existing stacking fault pyramids are annihilated, followed by an extended elastic deformation regime. The plastic deformation that follows the termination of the elastic behavior created extrinsic stacking faults, rather than the intrinsic stacking faults seen during loading. The onset of plastic deformation coincides with the maximum tensile force.

The molecular dynamics simulation results were then compared with experimental results [4,5] obtained using a compliant cantilever. This comparison required the conversion of the simulation results that corresponded to an experiment on a very stiff testing machine to the case of a very soft testing machine (cantilever beam experiment). For this type of experiment, the simulations show

very abrupt jumps in force or conductance and elastic deformation extended to larger displacements. The qualitative features of the force, contact area and conductance versus displacement plots are in excellent qualitative agreement with the extant experimental results. This includes the pronounced differences observed between loading and unloading. The simulations and experiments both show that Johnson–Kendall–Roberts theory should not be applied to describe asperity loading, but is applicable to the case of unloading, where the deformation is nearly elastic.

### Acknowledgements

This work was funded through the Materials Research Science and Engineering program of the National Science foundation, Grant DMR 0213706. P.C. gratefully acknowledges the partial support of the post-doctoral Fellowship Program of the Korea Science and Engineering Foundation (KOSEF).

### References

- [1] Yao JJ, Chang MF. In: Proc. IEEE Transducers'95; 1995. p. 384; Zhou S, Sun XQ, Carr WN. In: Proc. IEEE Transducers'97; 1997. p. 1137; Hyman D, Schmitz A, Warneke B, Hsu TY, Lam J, Brown J et al. Electron Lett 1999;35:224.
- [2] Kim C, Burrows PE, Forrest SR. Science 2000;288:831.
- [3] Pascual JI, Mendez J, Gomez-Herrero J, Baro AM, Garcia N, Binh VT. Phys Rev Lett 1993;71:1852; Pascual JI, Mendez J, Gomez-Herrero J, Baro AM, Garcia N, Landman U, et al. Science 1995;267:1793; J Vac Sci Technol B 1995;13:1280.
- [4] Agrait N, Rubio G, Vieira S. Phys Rev Lett 1995;74:3995.
- [5] Rubio G, Agrait N, Vieira S. Phys Rev Lett 1996;76:2302.
- [6] Stalder A, Dürig U. Appl Phys Lett 1996;68:637; J Vac Sci Technol B 1996;14:1259.
- [7] Olesen L, Laegsgaard E, Stensgaard I, Besenbacher F, Schiotz J, Stoltze P, et al. Phys Rev Lett 1994;72:2251.
- [8] Krans JM, van Ruitenbeek JM, Fisun VV, Yanson IK, de Jongh LJ. Nature (London) 1995;375:767, and references therein.
- [9] Costa-Krämer JL, García N, García-Mochales P, Serena PA. Surf Sci 1995;342:L1144; Costa-Krämer JL, García N, García-Mochales P, Serena PA, Margués MI, Correia A. Phys Rev B 1997;55:5416; Costa-Krämer JL. Phys Rev B 1997;55:R4875.
- [10] Landman U, Luedtke WD, Salisbury BE, Whetten RL. Phys Rev Lett 1996;77:1362.
- [11] Todorov TN, Sutton AP. Phys Rev Lett 1993;70:2138; Phys Rev B 1996;54:14234.
- [12] Bratkovsky AM, Sutton AP, Todorov TN. Phys Rev B 1995;52:5036.
- [13] Sørensen MR, Brandbyge M, Jacobsen KW. Phys Rev B 1998;57:3283.
- [14] Landman U, Luedtke WD, Burnham NA, Colton RJ. Science 1990;248:454.
- [15] Rafii-Tabar H, Kawazoe Y. Jpn J Appl Phys 1993;32:1394.
- [16] Van Vliet KJ, Li J, Zhu T, Yip S, Suresh S. Phys Rev B 2003;67:104105.
- [17] Rodríguez de la Fuente O, Zimmerman JA, González MA, de la Figuera J, Hamilton JC, Pai WW, Rojo JM. Phys Rev Lett 2002;88:036101-1.
- [18] Kelchner CL, Plimpton SJ, Hamilton JC. Phys Rev B 1998;58:11085.
- [19] Allen MP, Tildesley DJ. In: Computer simulation of liquids. New York: Oxford University Press; 1987.
- [20] Daw MS, Baskes I. Phys Rev B 1984;29:6443; Phys Rev Lett 1983;50:1285.
- [21] Foiles SM, Baskes MI, Daw MS. Phys Rev B 1986;33:7983.
- [22] Cai J, Ye YY. Phys Rev B 1996;54:8398.
- [23] Steinhard PJ, Nelson DR, Ronchetti M. Phys Rev B 1983;28:784; Chushak Y, Bartell LS. J Phys Chem A 2000;104:9328.
- [24] Vergeles M, Maritan A, Koplík J, Banavar JR. Phys Rev E 1997;56:2626.
- [25] Jansen AGM, van Gelder AP, Wyder P. J Phys C 1980;13:6073.
- [26] Torres JA, Pascual JI, Saenz JJ. Phys Rev B 1994;49:16581, We are not taking quantum size effects into account because the necks are wide enough to comprise many quantum channels, and the jumps observed in the conductance are always several quantum units high.
- [27] Sørensen MR, Jacobsen KW, Jónsson H. Phys Rev Lett 1996;77:5067.
- [28] Hirth JP, Lothe J. In: Theory of dislocations. New York: Wiley; 1982.
- [29] Quon RA, Knarr RF, Vanderlick TK. J Phys Chem B 1999;103:5320.
- [30] Adams GG. Private communication.
- [31] Johnson KL, Kendall K, Roberts AD. Proc R Soc Lond A 1971;324:301.
- [32] Majumder S, McGruer NE, Adams GG, Zavracky PM, Morrison RH, Krim J. Sensor Actuator A 2001;93:19.